JOURNAL OF SPACECRAFT AND ROCKETS
Vol. 34, No. 4, July–August 1997

High-Enthalpy Aerothermodynamics of a Mars Entry Vehicle Part 1: Experimental Results

Brian R. Hollis* and John N. Perkins†
North Carolina State University, Raleigh, North Carolina 27695-7910

Aerodynamic heating tests were conducted on a 70-deg sphere–cone Mars entry vehicle configuration in a high-enthalpy impulse facility in both carbon dioxide and air test gases. The purpose of these tests was to obtain heat transfer data for comparison with results of Navier–Stokes computations. Surface heat transfer rates were determined for both the forebody and afterbody of the test models and for the stings that supported the models in the facility test section. Little difference was observed between normalized heating distributions for the air and carbon dioxide test conditions. For both cases, peak sting heating was on the order of 4–5% of the forebody stagnation-point heating, and it was concluded that the wake flow remained laminar. The wake flow establishment process was quantified and was found to require approximately 40–70 flow path lengths, which corresponded to approximately 75% of the available facility test time. The repeatability of facility test conditions was estimated to vary between ± 3% and ± 10%. The overall experimental uncertainty of the data was estimated to be ± 10–11% for forebody heating and ± 17–22% for wake heating.

Nomenclature

B = measurement bias error
h = enthalpy, J/kg
k = thermal conductivity, W/m · K
M = Mach number
P = measurement precision error
p = pressure, N/m^2
q = heat transfer rate, W/m^2
R = radius, m
Re = Reynolds number
S = distance along model surface, m
T = temperature, K
t = time, s
U_∞ = freestream velocity, m/s
U_{tot} = total combined uncertainty
y_{ref} = reference length, m
α = thermal diffusivity, m^2/s
β = thermal product, $\alpha/\sqrt{k}$, W · s$^{1/2}$/m^2 · K
λ = correction factor, K^{-1}
ρ = density, kg/m^3
σ = heat transfer residual
τ = nondimensional time, $U_\infty \Delta t_{\text{est}}/y_{\text{ref}}$

Subscripts

est = establishment
w = wall
0 = stagnation
1 = freestream
2 = post-normal shock

Introduction

IN recent years, NASA has embarked on a long-term exploration initiative[1] in which unmanned orbiters and landers will be employed to gather scientific data on the planet Mars. This initiative has produced renewed interest in blunt-body entry vehicle and aerobrake configurations such as the 70-deg sphere–cone geometry of the Mars Pathfinder (formerly known as MESUR) spacecraft.[2] This interest has led to a number of computational and experimental studies of blunt-body flows[3–14] in perfect-gas, high-enthalpy, and rarefied environments.

The present study contributes to the growing database on blunt-body flows through the presentation of comparisons between blunt-body heat transfer rates measured in a high-enthalpy impulse facility and those obtained from flowfield solutions computed using a nonequilibrium Navier–Stokes solver. These experiments and computations were conducted with test gas environments (CO_2 and N_2–O_2) representative of the atmospheres of Mars and Earth and encompassed both the forebody and wake (that is, the afterbody and model sting) regions of the flow. The experimental data from this study are presented in Part 1 of this work, and the computational results are presented in Part 2 (Ref. 15).

The subject of this work was a 70-deg sphere–cone configuration derived from the geometry of the Mars Pathfinder spacecraft. This sphere–cone geometry is shown in Fig. 1; the locations of control points on the model and sting in terms of nondimensional distance from the forebody stagnation point, S/R_b, are also shown in Fig. 1. The radius of the sphere–cone forebody test model was 2.54 cm (1 in.). The forebody had a nose-radius/forebody-radius ratio of 0.5 and a corner-radius/forebody-radius ratio of 0.05. This configuration also had a 40-deg cone-frustum afterbody, which represented the payload section of the vehicle. The cone-frustum angle was altered from that of Mars Pathfinder (49.5 deg) to accommodate the sting that was used to support the model in the test facility. This change was considered to be acceptable, as the presence of the sting would alter the wake flowfield in any event. The sting was fitted to a 45-deg cone strut adapter. The adapter was mated to the sting at a point 4.6 forebody base radii downstream from the frustum, which was a sufficient distance to ensure that boundary-layer separation induced by the shock at the adapter would not influence the near-wake region of interest directly behind the model.

Whereas this research encompassed both the forebody and wake regions of the sphere–cone configuration, emphasis was placed on measurements and computations for the wake of the configuration. The important features of a blunt-body wake flowfield (Fig. 2) are as follows: a free shear layer formed by the separation of the forebody boundary layer at or around the corner of the vehicle; a recirculating flow region in the wake of the vehicle; a free-shear-layer impingement point on the sting (or a "neck" region in the case of actual spacecraft, which would not have a sting); and a recompression shock formed as the free shear layer is turned back into the direction of the freestream. These features define the aerothermodynamic environment of the wake, and their behavior influences the design of an aerobrake or entry vehicle. Thermal protection shielding on the payload of the vehicle must be sufficient to withstand the

Received Aug. 15, 1996; revision received March 2, 1997; accepted for publication March 15, 1997.

*Graduate Researcher, Department of Mechanical and Aerospace Engineering. Member AIAA.
†Professor, Department of Mechanical and Aerospace Engineering. Associate Fellow AIAA.

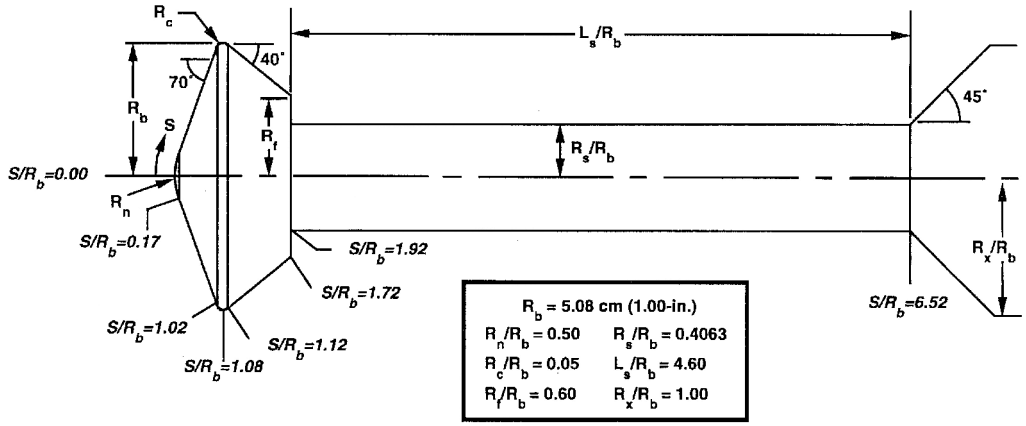

Fig. 1 Model and sting geometry.

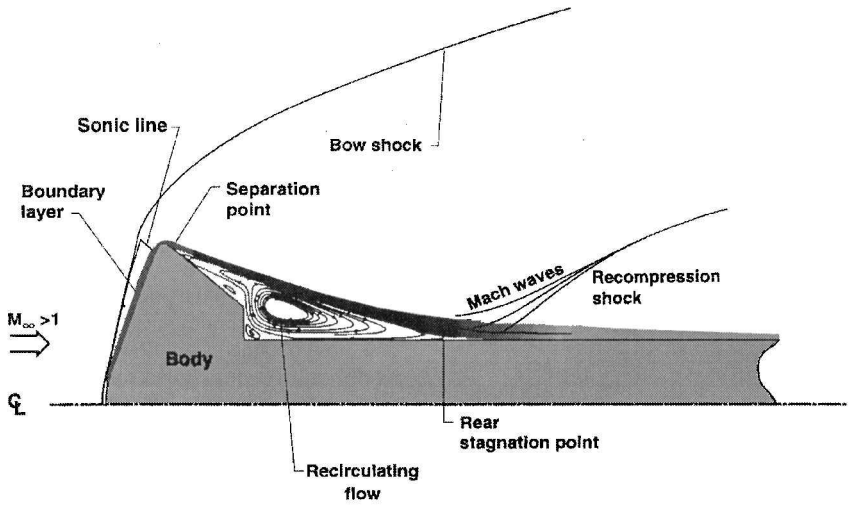

Fig. 2 Blunt-body wake flow structure.

aerothermodynamic loads imposed upon it, and the size and placement of the payload must be such that the wake free shear layer does not impinge upon it, or a localized region of high heating will be produced.

Aerothermodynamic Test Models

Aerothermodynamic test models (Fig. 3) of the 70-deg sphere–cone configuration were machined from Macor® (Corning, Inc.) ceramic. Model stings were fabricated from stainless steel, and a lengthwise slot was machined into each sting to accommodate a contoured Macor insert. Glass or ceramic materials such as quartz, Pyrex® (Corning Inc.), or Macor are commonly used in the construction of heat transfer models because they are thermal insulators, and thus the thermal penetration depth into a model fabricated from one of these materials is small. Because of this fact, a greater, and thus more easily measured, temperature rise is produced on the surface of the model. Furthermore, the substrate can be treated as being of semi-infinite thickness: that is, the thermal penetration depth of the heat load into the substrate is much less than the thickness of the model skin. This assumption is required in the development of several of the methods commonly employed for the computation of surface heating rates from measured temperature time-history data. In this study, Macor was chosen as the material for the models over quartz or Pyrex because it is more easily machined than quartz and because it exhibits smaller variations in thermal properties with temperature than Pyrex.

The sphere–cone models and the model sting inserts were instrumented with thin-film temperature resistance gauges (following the procedure described in Ref. 16), which were used to measure temperature time histories on the models' surfaces. A thin-film gauge is an approximately 1000-Å-thick palladium sensing element, which is applied to a model either through a metal deposition process or

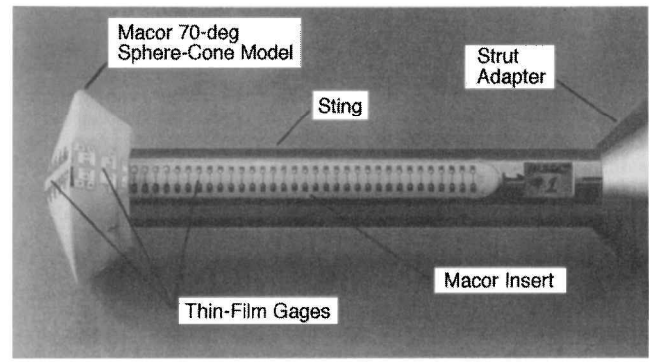

Fig. 3 Test model.

by hand painting. Most of the gauges on the models were applied through deposition; gauges were hand painted only in regions of extreme surface curvature, such as the corners of the sphere–cone models, where deposition was impractical. Typical gauge resistances were on the order of 100–150 Ω. Gauges were coated with a thin layer of Al_2O_3 to protect them from electrical shorting due to any ionization in the acceleration gas. The combined thickness of the sensor and overlayer was much less than the thermal penetration depth into the substrate, and therefore it could be assumed that they had a negligible effect on the heat transfer to the model. The sphere–cone models each had 37 thin-film gauges, while the Macor sting inserts had an additional 33. The gauge arrangement produced a surface spacing of approximately 2.5 mm (0.1 in.) and provided a continuous line of instrumentation covering the forebody, afterbody, and model sting (Fig. 3).

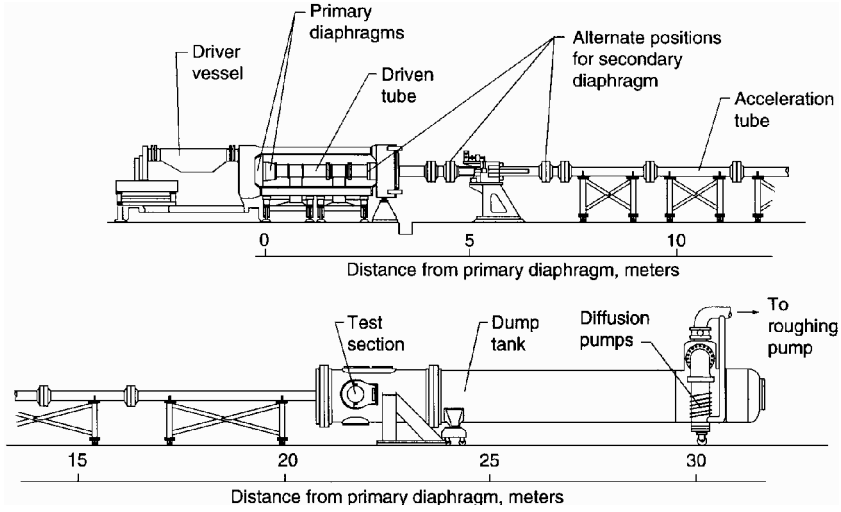

Fig. 4 HYPULSE Expansion Tube.

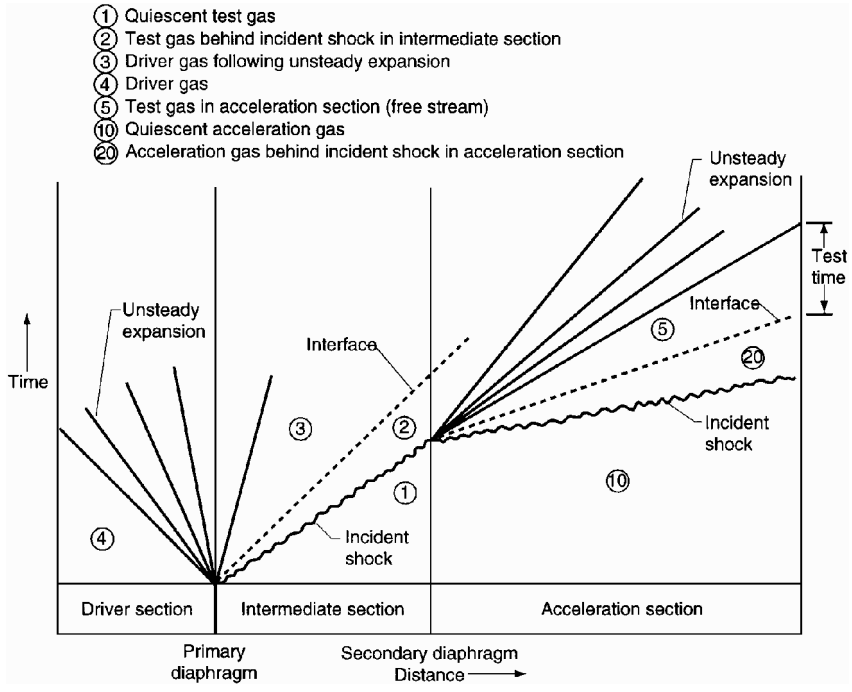

Fig. 5 Distance–time diagram for HYPULSE.

Facility Description

Aerothermodynamic testing of the entry-vehicle models was performed in the NASA HYPULSE Expansion Tube,[17] which is operated by the General Applied Sciences Laboratories of Ronkonkoma, New York (HYPULSE was previously operated by the NASA Langley Research Center). HYPULSE is an impulse facility in which hypervelocity, high-enthalpy flows can be produced using a variety of test gases. HYPULSE is used in the study of high-temperature, chemically reacting internal and external flows, such as that inside a scramjet[18] or around a planetary entry vehicle.[19] Data from studies such as these can match or be extrapolated to flight conditions, or can be employed in the validation of computational fluid dynamics codes.

The HYPULSE Expansion Tube (Fig. 4) has an internal diameter of 15.24 cm (6 in.), has a length of 30 m, and is divided into three sections: driver, intermediate (driven), and acceleration. The driver section is filled with highly pressurized helium gas and is separated by a steel double-diaphragm from the lower-pressure intermediate section, which is filled with the desired test gas. A Mylar® diaphragm divides the intermediate section from the acceleration section, which is filled with test gas at even lower pressure. A HYPULSE run is initiated by bursting the steel double-diaphragms, which produces a supersonic shock-tube flow in the intermediate section. When the incident shock wave reaches the end of the intermediate section, the Mylar diaphragm bursts, and a hypervelocity, high-enthalpy, hypersonic flow is produced as the test gas expands into the acceleration section. Models are positioned at the end of the acceleration section, where the expansion tube exits into an enclosed test section. This operating sequence is represented by the distance–time (X–T) diagram in Fig. 5.

This expansion-tube mode of operation is unique in that a high-enthalpy flow is produced with a freestream that is nearly free of chemical dissociation. This is in contrast to reflected-shock tunnels, in which the flow is stagnated and then processed by a shock wave in order to generate the desired high enthalpy and velocity. The reflected-shock method of operation produces a high-enthalpy flow that has a greater test time than an expansion tube flow but does so at the expense of some test-gas dissociation.

Test Conditions

HYPULSE has a variety of operating points in which air, CO_2, He, N_2, or O_2 can be employed as test gases. In this study, operation of HYPULSE was limited to the conditions listed in Table 1, which are referred to as the Langley conditions, as they are derived

Table 1 HYPULSE test conditions

Test gas	ρ_1, kg/m^3	U_1, m/s	T_1, K	P_1, Pa	$h_0 - h_{298K}$, MJ/kg	$P_{0,2}$, MPa	$T_{0,2}$, K
CO_2	0.00579	4772	1088	1187	12.25	0.130	3700
	±3.1%	±1.1%	±8.7%	±10.8%	±2.1%	±1.8%	±0.9%
Air	0.00571	5162	1113	1824	14.18	0.147	6027
	±1.8%	±0.9%	±9.3%	±9.9%	±1.4%	±1.3%	±0.8%

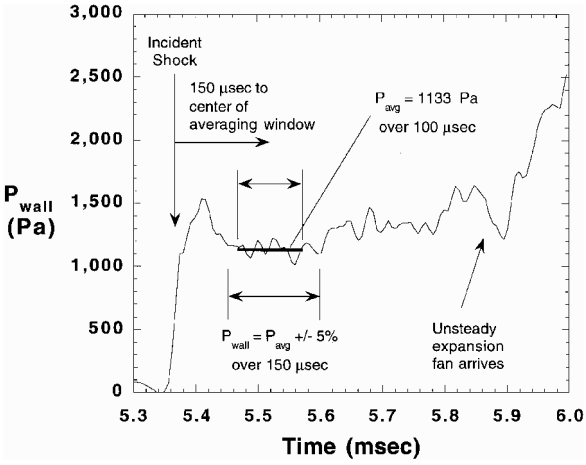

Fig. 6 Typical wall pressure data for CO_2 test.

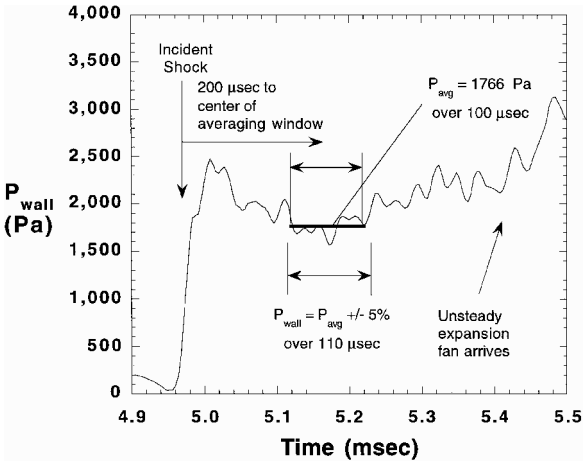

Fig. 7 Typical wall pressure data for air test.

from those at which tests were conducted when the facility was operated by the NASA Langley Research Center. Conclusions drawn in this paper should be interpreted as referring only to those conditions and not to the overall capabilities of the HYPULSE Expansion Tube. Detailed calibration studies have been performed at the Langley conditions.[20] For both air and CO_2, pitot pressure surveys at the exit of the expansion tube have identified an inviscid test core of approximately 7.6-cm (3-in.) diam over which the pitot pressure is constant to within ±6%. At the Langley conditions, nominal steady-flow test times have been determined from pitot and tube wall pressure data to be on the order of 250 μs.

In this work, the actual steady-flow test period of each run was determined by examination of wall pressure data (the presence of the test model left no room for a pitot probe). Because surface heating rates were observed to be very sensitive to variations in the freestream conditions, a small acceptable magnitude of deviation in the wall pressure was stipulated, and consequently the accepted test durations were shorter than the nominal times. Typical wall pressure time histories for CO_2 and air runs are shown in Figs. 6 and 7. To determine the steady-state run duration, the wall pressure was first averaged over a 100-μs interval centered 150 μs from the arrival of the incident shock wave for CO_2 or 200 μs from the incident shock wave for air. The total test period was then taken to be the time over

Table 2 HYPULSE simulation parameters

Test gas	M_1	$Re_{1,d}$	Kn_1	ρ_2/ρ_1
CO_2	9.71	3.35×10^4	0.00037	18.98
Air	7.93	3.39×10^4	0.00028	10.98

which the wall pressure varied by no more than ±5% from the average value over the 100-μs interval. Based on the application of this criterion to all of the CO_2 and air runs conducted in this research, the average steady-state run duration for heat transfer testing at the Langley conditions was found to be 150 μs for CO_2 and 125 μs for air. These values are more conservative than the quoted nominal values, but, as the heating data were intended for comparison with computational results, the ±5% criterion was imposed to minimize the uncertainty in the freestream flow conditions.

The flow conditions for each run were computed using the Equilibrium Reacting Gas (ERGAS) code.[21] Inputs required for this code are the freestream velocity, the pitot pressure, and the freestream static pressure. The freestream velocity was assumed to be equal to the incident shock velocity, which was computed for each run from the time required for the pressure disturbance caused by the incident shock to travel between wall pressure measurement stations in the expansion tube. The freestream pressure was assumed to be equal to the time-averaged wall pressure measured immediately upstream of the end of the expansion tube, whereas the pitot pressure was taken from calibrations of the facility wall pressure against the pitot pressure. The mean values for the flow properties based on the data from all the runs are listed in Table 1. Nondimensional simulation parameters for these test conditions are listed in Table 2.

Uncertainty estimates for the run-to-run repeatability of test flow conditions are also given in Table 1. The uncertainties are estimated as two standard deviations of the individual properties from their mean values, as based on the data from all of the runs at each test condition. The test conditions were found to be quite repeatable in this test series. In both test gases, the greatest uncertainty was in the freestream pressure, which was estimated to vary by ±10%, whereas the freestream density and velocity, which are the factors that have the greatest influence on aerodynamic heating, were estimated to have uncertainties of no more than ±3%.

Data Acquisition and Reduction

Data acquisition in the HYPULSE Expansion Tube is performed with a LeCroy Model 6810 waveform digitizer, which is capable of processing 152 channels of data, of which 10 are reserved for facility use. For aerothermodynamic testing, thin-film gauge current is supplied by LAMBDA type LQ411 low-noise linear power supplies through GASL-manufactured, 20-channel, floating-ground-point gauge control units. In these tests, gauge current was supplied at a constant 1 mA, which was sufficiently low to minimize ohmic heating of the gauges. The data sampling rate for the present work was 500 kHz.

Test data were in the form of voltage time histories for each of the thin-film gauges, which were converted to temperature time histories using prior voltage–temperature calibrations and gauge resistance measurements. The temperature time histories were then input into the 1DHEAT data reduction code,[22] which was used to compute the heat transfer rates.

Three different data reduction schemes, all of which are based on the assumption of one-dimensional heat conduction[23] into the model substrate, are incorporated into the 1DHEAT code. The first two, the classic Cook–Felderman technique[24] and the related Kendall–Dixon technique,[25,26] are analytical methods in which the assumption of

heat conduction to a semi-infinite solid with constant thermal properties is used to derive closed-form solutions for the heating rates. The third technique is a numerical solution of the one-dimensional finite volume heat conduction problem.

In the Cook–Felderman method, which is also referred to as the direct method, the heat transfer rate is computed from the temperature time history via

$$q(t_n) = \frac{2\beta}{\sqrt{\pi}} \sum_{i=1}^{i=n} \frac{T_i - T_{i-1}}{\sqrt{t_n - t_i} + \sqrt{t_n - t_{i-1}}} \tag{1}$$

where

$$\beta = \sqrt{\rho c_p k} \tag{2}$$

is the thermal product of Macor. The value used for β at room temperature was 1642 $W \cdot s^{1/2}/m^2 \cdot K$ (Ref. 22).

In the Kendall–Dixon method, which is also referred to as the indirect method, the total heat energy added to the model as a function of time is first computed from

$$Q(t_n) = \frac{\beta}{\sqrt{\pi}} \sum_{i=1}^{n} \frac{(T_i - T_1) + (T_{i-1} - T_1)}{\sqrt{t_n - t_i} + \sqrt{t_n - t_{i-1}}} \Delta t \tag{3a}$$

The time history of the heat transfer rate is then computed from

$$q(t_n) = \frac{dQ_n}{dt} = \frac{-2Q_{i-8} - Q_{i-4} + Q_{i+4} + 2Q_{i+8}}{40\,\Delta t} \tag{3b}$$

Over a given time interval, the direct and indirect methods will yield nearly identical time-averaged values. However, the instantaneous heating rates are quite different, because the wide four-point differencing stencil in Eq. (3b) tends to dampen fluctuations in the time history. This behavior is illustrated in Fig. 8 with sample heat transfer data from HYPULSE. Although the indirect method is useful for reducing experimental noise, its use would not be recommended if transient phenomena such as turbulence were of interest. The indirect method was preferred in this work because only the steady-state heating rates (or quasisteady in regard to the flow establishment process) were of interest.

Both Eqs. (1) and (3) were derived with the assumption of constant material thermal properties. However, materials commonly used in the construction of heat transfer models, such as quartz, Pyrex, or, in this case, Macor, do exhibit a dependence on temperature. Thus, because of the high temperatures produced in a model exposed to a hypersonic flow, direct application of these methods can result in large errors. To deal with this problem, an empirical correction factor for the effects of Macor thermal properties was derived,[22] which has the form

$$q_{\text{var}} = q_{\text{const}}(1 + \lambda\,\Delta T_w) \tag{4}$$

where λ is the correction factor, ΔT_w is the increase in surface temperature from ambient room temperature, and q_{const} is the value

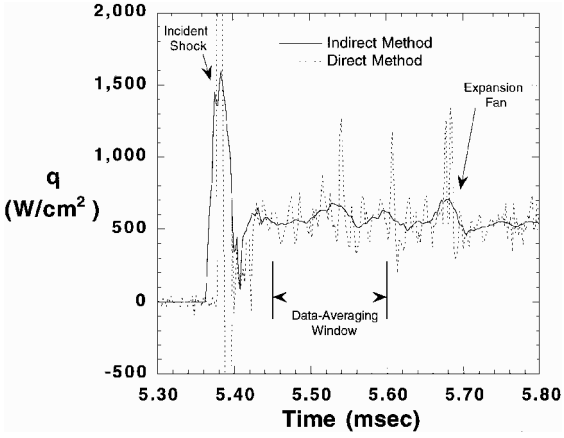

Fig. 8 Comparison of heat transfer rates from indirect and direct methods.

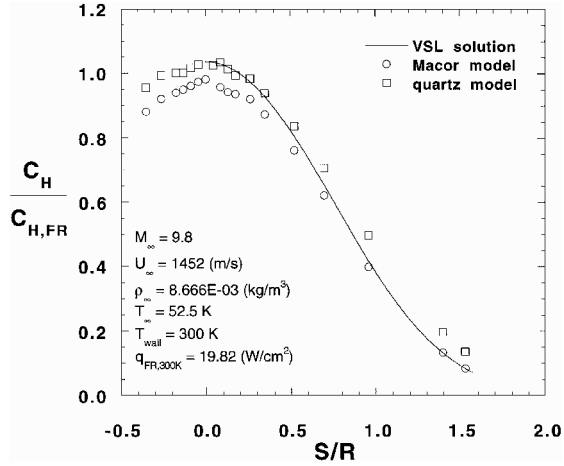

Fig. 9 Heating data from Macor calibration tests.

computed using either Eq. (1) or Eq. (3). The correction factor is given by

$$\lambda = 7.380 \times 10^{-4} - 4.604 \times 10^{-7}\,\Delta T_w \tag{5}$$

This empirical method has proven to be very accurate[22] and is useful for rapid real-time analysis of experimental data. However, for a more rigorous analysis of heating data, a numerical solution of the one-dimensional heat conduction equation should be performed. In 1DHEAT, a numerical solution is computed via an implicit one-dimensional finite volume technique. In a numerical solution, the semi-infinite assumption is not required, and the variation of thermal properties with temperature is incorporated into the formulation of the technique. Boundary conditions for the numerical solution are the measured surface temperature time history on the exterior of the model and an adiabatic boundary at the interior of the model. The correction factor in Eq. (4) for the analytical methods was derived by comparison of constant-properties solutions from Eqs. (1) and (3) to finite volume solutions. In this study, the indirect method was used for initial analysis of the data during the test series, and the finite volume method was used to verify these results after the test series was completed.

At present, the following curve fits[22] for Macor thermal properties (which are based on new data) for temperatures up to 600 K are recommended for use in numerical solutions:

$$\rho = 2543.84\ \text{kg/m}^3 \tag{6}$$

$$k = 0.33889 + 7.4682 \times 10^{-3}T - 1.6118 \times 10^{-5}T^2 + 1.2376 \times 10^{-8}T^3\ \text{W/m} \cdot \text{K} \tag{7}$$

$$\alpha = 1.3003 \times 10^{-6} - 2.2523 \times 10^{-9}T + 1.8571 \times 10^{-12}T^2\ \text{m}^2/\text{s} \tag{8}$$

The validity of these curve fits was assessed in tests[4] on a 5.08-cm (2-in.) diam Macor hemisphere in the LaRC 31-Inch Mach 10 Air Tunnel,[27] a facility in which chemical reactions are not a concern because of the low total enthalpy levels and which is known for its high flow uniformity. Stanton numbers computed from heat transfer measurements were compared with both viscous shock layer (VSL) calculations[28] and Stanton number values measured on an identical quartz hemisphere, which was tested simultaneously with the Macor hemisphere. These values were all normalized by the stagnation-point Stanton number computed using the Fay–Riddell[29] method. Sample data from these tests are shown in Fig. 9. In all tests, the Macor hemisphere results were within 5% of both the quartz and VSL values, and were within 3% of the Fay–Riddell values. That suggests that these curve fits are reasonably accurate at least up to the stipulated temperature limit.

Wake Flow Establishment

The forebody heat transfer rates reported herein are simply time averages of the values obtained over the entire steady-flow test window. However, the determination of the heat transfer rates for the

afterbody and model sting was somewhat more complicated because of the transient nature of the flow establishment process. Whereas the forebody flow establishment process is fairly rapid (25–50 μs in HYPULSE), the time required for the flow in the wake of a blunt body, such as the 70-deg sphere–cone configuration, can amount to a significant fraction of the total test time available in an impulse facility. During this establishment process, there are large fluctuations in both the magnitude and the shape of the wake heating distributions. It is therefore necessary to determine at what point the wake flowfield has become fully established in order to determine the time interval over which to average the heating rates.

To determine when the wake flow can be considered to be established, an establishment criterion based on the change in the measured heat transfer rates between sample times was defined.[4] This heat transfer residual is defined by

$$\sigma(t) = \left|\frac{\Delta q(t)}{q(t)}\right| = \left|\frac{q(t_i) - q(t_{i-1})}{q(t_i)}\right| \tag{9}$$

and is computed for each gauge. To characterize the entire wake region with a single variable, the root-mean-square (rms) variation of all the wake gauge residuals is then computed at each sample time by

$$\text{rms}(\sigma) = \sqrt{(1/n)\left(\sigma_1^2 + \sigma_2^2 + \cdots + \sigma_n^2\right)} \tag{10}$$

The time history of the residual rms can be used to identify the established flow period and to locate the arrival time of features of the expansion-tube wave system, as shown in Fig. 10. Based on examination of time histories of both the heat transfer rates and the overall heat transfer distributions, it was concluded that the wake flow could be considered to be established when the rms had dropped below a value of $\approx$0.02. In regard to the use of Eq. (10), it should be pointed out that heat transfer gauges that are behaving poorly, i.e., those that produce an extremely noisy signal due to gauge damage or bad electrical connections, should not be included in the rms computation, or the results will be skewed by the noise from them.

The rms criterion was applied to each run, and nondimensional flow establishment times for the 70-deg sphere–cone wake flow were calculated from

$$\tau = \frac{U_\infty \, \Delta t_{\text{est}}}{y_{\text{ref}}} \tag{11}$$

In Eq. (11), Δt_{est} is defined as the time from the arrival of the incident shock, and y_{ref} is defined as the difference between the forebody radius and the sting radius. The time τ varied from 40 to 70 with an average value of 51 in the CO_2 tests and varied from 50 to 90 with an average value of 65 in the air tests. These values are consistent with previous studies[30] and represent, for either gas, approximately 75% of the total time from the arrival of the incident shock to the end of the test period.

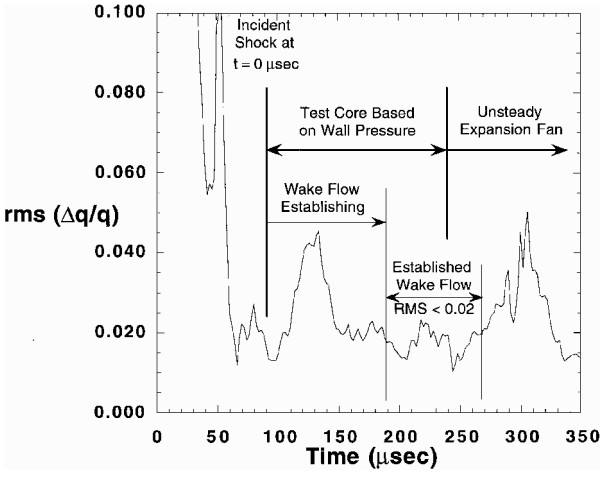

Fig. 10 Wake residual rms time history.

Experimental Results

Heat transfer data are presented in Figs. 11 and 12 for CO_2 and Figs. 13 and 14 for air, and a comparison of the air and CO_2 results is presented in Fig. 15. In Figs. 11 and 13, the forebody and wake data are plotted on separate linear axes to emphasize the details in both regions. In Figs. 12 and 14, the data are plotted on a single continuous logarithmic scale to emphasize the relative magnitudes of the forebody and wake heating. Several runs were made in each test gas to verify the repeatability of the results, and the data from

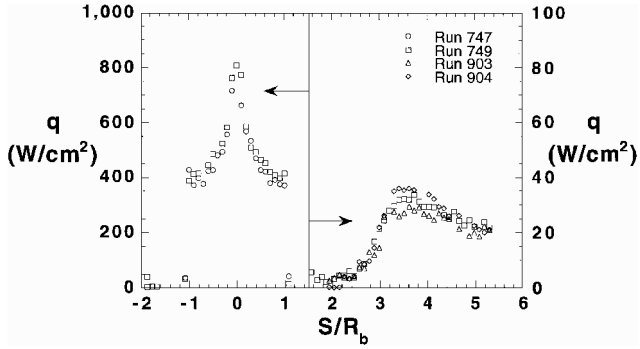

Fig. 11 Seventy-degree sphere–cone heating data at CO_2 test condition, linear scales.

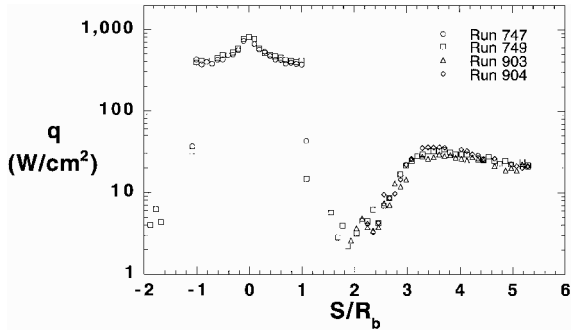

Fig. 12 Seventy-degree sphere–cone heating data at CO_2 test condition, logarithmic scale.

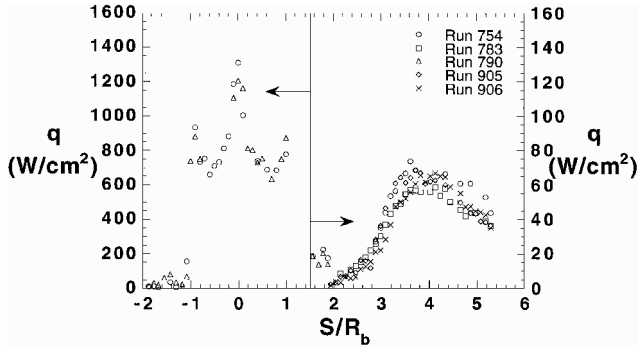

Fig. 13 Seventy-degree sphere–cone heating data at air test condition, linear scales.

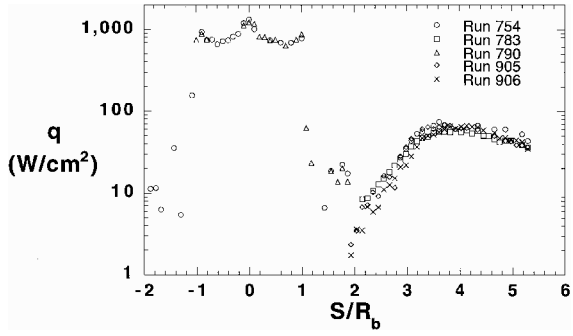

Fig. 14 Seventy-degree sphere–cone heating data at air test condition, logarithmic scale.

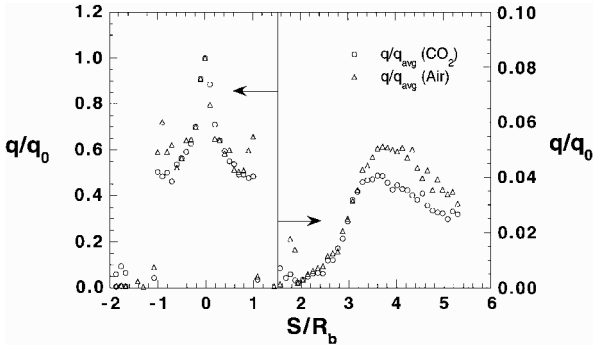

Fig. 15 Comparison of normalized heating distributions for CO_2 and air test cases.

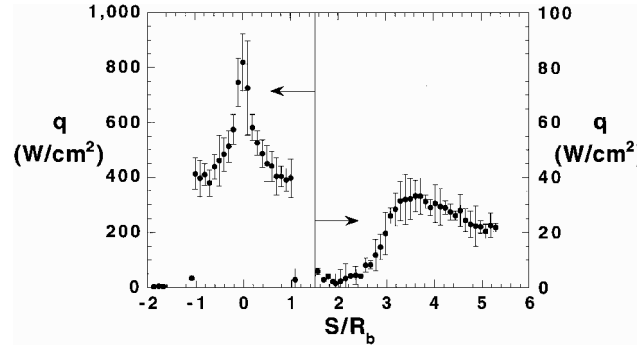

Fig. 16 Seventy-degree sphere–cone heating at CO_2 test condition: mean values and uncertainty estimates.

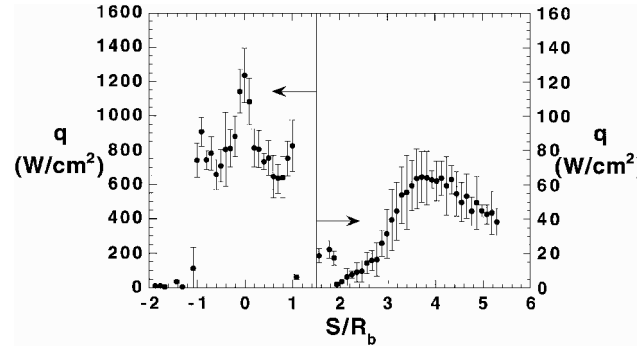

Fig. 17 Seventy-degree sphere–cone heating at air test condition: mean values and uncertainty estimates.

each of these runs are presented in each of these figures. Averaged values of the surface heating distributions from all the runs for each case are used for the comparison in Fig. 15. These distributions are normalized by the respective measured stagnation-point heating rates for the purpose of comparison.

As shown in Figs. 11–14, forebody stagnation point heat transfer rates were approximately 810 W/cm^2 in CO_2 and 1250 W/cm^2 in air. Local heating maxima were observed at the forebody corners in the air tests but were not observed in the CO_2 tests. The gauge spacing on the model corners was apparently not close enough to resolve these narrow corner heating maxima for this case.

In both test gases, afterbody and sting heating rates were at least two orders of magnitude lower than those on the forebody (Figs. 11–14). In air, the peak sting heating was 5% of that at the forebody stagnation point, and was 4% of that in CO_2. Sting peak heating rates of these magnitudes are consistent with laminar wake flow[11–14]; in contrast, peak sting heating rates of 15–30% of that at the forebody stagnation point can be experienced in turbulent wake flows.[3–6,13] Comparisons in Part 2 of this study[15] of the experimental data with laminar computational results further support the theory that the wake flow remained laminar for the HYPULSE test cases.

Whereas small differences between the normalized CO_2 and air distributions due to the different shock density ratios can be seen in the computational results presented in Part 2 of this study,[15] the differences in the experimental data (Fig. 15) were within the experimental uncertainty except on the sting downstream of the peak heating point, where the distribution in air was slightly higher than that in CO_2. As discussed in Part 2, the chemical and vibrational processes in the wake are frozen by the rapid expansion of the flow around the forebody corner for both cases.

Uncertainty Analysis

The combined total uncertainty of the heat transfer measurements was estimated by[31]

$$U_{\text{tot}} = t_{95}\sqrt{B^2 + P^2} \tag{12}$$

In Eq. (12), t_{95} represents the 95th percentile point of the two-tailed Student's t distribution. The value of t_{95} depends on the number of measurements made of a quantity, and approaches 2 in the limit of an infinite number of data points. However, according to Ref. 31, $t_{95} = 2$ is an acceptable standard regardless of the number of data points. The experimental bias error B was assumed to be dominated by error due to the uncertainty in the thermal properties. Based on the hemisphere tests in the 31-Inch Mach 10 Air Tunnel and using the Fay–Riddell heat transfer computations as a reference standard, the bias error was estimated to be ±3%. Mean values of the heat transfer rates were computed from the data from each of the repeat runs at the air and CO_2 test conditions. The experimental precision error was taken to be equal to the standard deviation of the data from these mean values.

Uncertainty estimates were made for the data from each gauge position. The average estimated values for the combined total uncertainty were ±11% on the forebody and ±17% on the afterbody and sting for the CO_2 data; for the air data, the average values were ±12% on the forebody and ±22% on the afterbody and sting. The greater uncertainty for the wake data was due to the fact the wake heating rates were at least two orders of magnitude lower than the forebody ones, and thus a greater precision error was produced by the higher signal-to-noise ratio of the wake data. The individual uncertainty bounds computed for each gauge position are shown along with the average heat transfer rates in Fig. 16 for CO_2 and in Fig. 17 for air.

Summary and Conclusions

A series of high-enthalpy aerothermodynamic tests has been conducted on a Mars entry vehicle configuration in the HYPULSE Expansion Tube in both CO_2 and air test gases. In these tests, the magnitude of run-to-run variations in individual flow conditions was no greater than ±10% and was less than ±3% for freestream velocity and density. Steady-flow test times in this facility were estimated to be 150 μs in CO_2 and 125 μs in air. Heat transfer measurement uncertainty was estimated to be ±11% on the forebody and ±17% in the wake for CO_2 tests, and ±12% on the forebody and ±22% in the wake for air tests. Forebody stagnation point heat transfer rates were 810 W/cm^2 in CO_2 and 1250 W/cm^2 in air. The wake flow establishment process was investigated, and it was found that approximately 75% of the total test time was required for a steady wake flow to be established. Afterbody and sting heating rates were at least two orders of magnitude lower than at the forebody stagnation point. The peak sting heating was equal to approximately 4% of the stagnation-point heating in CO_2 tests and 5% in air tests, and it was concluded that the wake remained laminar for both cases.

Acknowledgments

This research was conducted under NASA Grants NAGW-1331 and NAG1-1663 to North Carolina State University. Funding for model fabrication and testing in HYPULSE was provided by the Aerothermodynamics Branch, NASA Langley Research Center. The authors wish to thank John Calleja of General Applied Sciences Laboratories for his assistance in the HYPULSE tests and Roop Gupta of NASA Langley Research Center for the hemisphere VSL solutions.

References

[1]Bourke, R. D., Golombek, M. P., Spear, A. J., and Sturms, F. M., "MESUR and Its Role in an Evolutionary Mars Exploration Program,"

International Astronautical Federation, IAF Paper 92-0509, Paris, Sept. 1992.

[2]Wercinski, P. F., "Mars Aerocapture Analysis for the MESUR/Mars-Pathfinder Aeroshell in Low L/D Configurations," AIAA Paper 95-3495, Aug. 1995.

[3]Hollis, B. R., and Perkins, J. N., "High-Enthalpy and Perfect-Gas Heating Measurements on a Blunt Cone," *Journal of Spacecraft and Rockets*, Vol. 33, No. 5, 1996, pp. 628–635.

[4]Hollis, B. R., "Experimental and Computational Aerothermodynamics of a Mars Entry Vehicle," Ph.D. Dissertation, Dept. of Mechanical and Aerospace Engineering, North Carolina State Univ., Raleigh, NC, Dec. 1996; also NASA CR 201633, Dec. 1996.

[5]Horvath, T. J., McGinley, C. B., and Hannemann, K., "Blunt Body Near Wake Flow Field at Mach 6," AIAA Paper 96-1935, June 1996.

[6]Horvath, T. J., and Hannemann, K., "Blunt Body Near Wake Flow Field at Mach 10," AIAA Paper 97-0986, Jan. 1997.

[7]Kastell, D., Horvath, T. J., and Eitelberg, G., "Nonequilibrium Flow Expansion Around a Blunted Cone," 2nd European Symposium on Aerothermodynamics, European Space Research and Technology Centre (ESTEC), Noordwijk, The Netherlands, Nov. 1994.

[8]Mitchletree, R. A., and Gnoffo, P. A., "Wake Flow About a MESUR Mars Entry Vehicle," AIAA Paper 94-1958, June 1994.

[9]Haas, B. L., and Venkatapathy, E., "Mars Pathfinder Computations Including Base-Heating Predictions," AIAA Paper 95-2086, June 1995.

[10]Gochberg, L. A., Allen, G. A., Gallis, M. A., and Deiwert, G. S., "Comparison of Computations and Experiments for Nonequilibrium Flow Expansions Around a Blunted Cone," AIAA Paper 96-0231, Jan. 1996.

[11]Allegre, J., and Bisch, D., "Blunted Cone at Rarefied Hypersonic Conditions. Experimental Density Flow Fields, Heating Rates and Aerodynamic Forces," Centre National de la Recherche Scientifique, CNRS Rept. RC 95-2, Meudon, France, Sept. 1995.

[12]Holden, M., Kolly, J., and Chadwick, K., "Calibration, Validation and Evaluation Studies in the LENS Facility," AIAA Paper 95-0291, Jan. 1995.

[13]Holden, M., Harvey, J., Boyd, I., George, J., and Horvath, T., "Experimental and Computational Studies of the Flow over a Sting Mounted Planetary Probe," AIAA Paper 97-0768, Jan. 1997.

[14]Moss, J. N., Price, J. M., Dogra, V. K., and Hash, D. B., "Comparison of DSMC and Experimental Results for Hypersonic External Flows," AIAA Paper 95-2028, June 1995.

[15]Hollis, B. R., and Perkins, J. N., "High-Enthalpy Aerothermodynamics of a Mars Entry Vehicle Part 2: Computational Results," *Journal of Spacecraft and Rockets*, Vol. 34, No. 4, 1997, pp. 457–463.

[16]Miller, C. G., "Comparison of Thin-Film Resistance Heat Transfer Gages with Thin-Skin Transient Calorimeter Gages in Conventional Hypersonic Wind Tunnels," NASA TM 83197, Dec. 1981.

[17]Tamagno, J., Bakos, R., Pulsonetti, M., and Erdos, J., "Hypervelocity Real Gas Capabilities of GASL's Expansion Tube (HYPULSE) Facility," AIAA Paper 90-1390, June 1990.

[18]Bakos, R., Tamagno, J., Rizkalla, O., Pulsonetti, M., and Chinitz, W., "Hypersonic Mixing and Combustion Studies in the GASL HYPULSE Facility," AIAA Paper 90-2095, June 1990.

[19]Calleja, J., Trucco, R., Tamagno, J., and Erdos, J., "Results of Hypervelocity Aeroheating Tests of Aeroassist Flight Experiment (AFE) Forebody Models in Air, Helium, and CO_2," General Applied Sciences Labs., GASL TR 326, Ronkonkoma, NY, Oct. 1990.

[20]Calleja, J., Tamagno, J., and Erdos, J., "Calibration of the GASL 6-Inch Expansion Tube (HYPULSE) for Air, Helium, and CO_2 Test Gases," General Applied Sciences Labs., GASL TR 325, Ronkonkoma, NY, Sept. 1990.

[21]Miller, C. G., "Computer Program of Data Reduction Procedures for Facilities using CO_2–N_2–O_2–Ar Equilibrium Real-Gas Mixtures," NASA TMX-2512, March 1972.

[22]Hollis, B. R., "User's Manual for the One-Dimensional Hypersonic Aero-Thermodynamic (1DHEAT) Data Reduction Code," NASA CR 4691, Aug. 1995.

[23]Schultz, D. L., and Jones, T. V., "Heat Transfer Measurements in Short-Duration Hypersonic Facilities," AGARD Rept. AG-165, Feb. 1973.

[24]Cook, W. J., and Felderman, E. J., "Reduction of Data from Thin-Film Heat Transfer Gages: A Concise Technique," *AIAA Journal*, Vol. 4. No. 3, 1966, pp. 561, 562.

[25]Kendall, D. N., Dixon, W. P., and Schulte, E. H., "Semiconductor Surface Thermocouples for Determining Heat Transfer Rates," *IEEE Transactions on Aerospace and Electronic Systems*, Vol. AES-3, No. 4, 1967, pp. 596–603.

[26]Hedlund, E. R., Hill, J. A. F., Ragsdale, W. C., and Voisinet, R. L. P., "Heat Transfer Testing in the NSWC Hypervelocity Wind Tunnel Utilizing Co-Axial Surface Thermocouples," U.S. Naval Surface Warfare Center, NSWC Rept. MP 80-151, Silver Spring, MD, March 1980.

[27]Micol, J. R., "Hypersonic Aerodynamic/Aerothermodynamic Testing Capabilities at Langley Research Center: Aerothermodynamic Facilities Complex," AIAA Paper 95-2107, 1995.

[28]Gupta, R. N., Lee, K.-P., and Zoby, E. V., "Enhancements to Viscous-Shock-Layer Technique," *Journal of Spacecraft and Rockets*, Vol. 30, No. 4, 1993, pp. 404–413.

[29]Fay, J. A., and Riddell, F. R., "Theory of Stagnation Point Heat Transfer in Dissociated Air," *Journal of the Aeronautical Sciences*, Vol. 25, No. 2, 1958, pp. 73–85.

[30]Holden, M. S., "Development and Code Evaluation Studies in Hypervelocity Flows in the LENS Facility," 2nd European Symposium on Aerothermodynamics for Space Vehicles, European Space Research and Technology Centre (ESTEC), Noordwijk, The Netherlands, Nov. 1994.

[31]"Assessment of Wind Tunnel Data Uncertainty," AIAA Standards Publication S-071, AIAA, Washington, DC, 1995.

B. A. Bhutta
Associate Editor